Contents lists available at ScienceDirect

Applied Materials Today

journal homepage: www.elsevier.com/locate/apmt



Exceptional fatigue-resistant austenitic stainless steel for cryogenic applications

Chetan Singh ^a, Taeho Lee ^a, Keun Hyung Lee ^a, You Sub Kim ^a, E-Wen Huang ^b, Jayant Jain ^c, Peter K. Liaw ^d, Soo Yeol Lee ^{a,*}

- ^a Department of Materials Science and Engineering, Chungnam National University, Daejeon, 34134, Korea
- ^b Department of Materials Science and Engineering, National Yang Ming Chiao Tung University, Hsinchu, 30013, Taiwan
- ^c Department of Materials Science and Engineering, Indian Institute of Technology, New Delhi, 110016, India
- ^d Department of Materials Science and Engineering, The University of Tennessee, Knoxville, TN 37996, USA

ARTICLE INFO

Keywords: Ultra-low temperature High cycle fatigue Phase transformation Cryogenic mechanical behavior Austenitic stainless steel

ABSTRACT

Most alloys change from ductile to brittle at cryogenic temperatures, whereas high-entropy alloys show better strength, ductility, and toughness. However, they suffer from cost and mass-production challenges. We discerned the fatigue behaviour of a cost-effective austenitic stainless steel, SS316L, at an ultra-low temperature (ULT) of 15 K. For the cryogenic applications, our work demonstrates that compared to room-temperature (RT), ULT exhibits eight times higher fatigue life, despite even higher applied stress [$\sigma_{\max} = 1.3 \times \sigma_{ys_{RT/ULT}}$ (280 MPa_{RT}; 517 MPa_{15 K})]. At 15 K, the fatigue mechanisms involve stacking faults, a two-step martensitic phase transformation ($\gamma \rightarrow \epsilon \rightarrow \alpha'$) and α' -martensite twinning, utilizing the applied fatigue strain efficiently. The remarkable improvement in the mechanical strength and fatigue life at ULT is the key to revolutionizing sustainable advancements in space exploration and energy storage.

1. Introduction

Materials science is inherently concerned with understanding the performance of materials under extreme conditions, e.g., ultra-low temperatures (ULTs), which are crucial in applications ranging from aerospace components to cryogenic equipment. While newly developed medium- and high-entropy alloys are promising, they suffer from cost and mass-production challenges [1–9]. In contrast, austenitic stainless steels have earned their place in engineering due to their ease of mass production, strength, and fracture toughness, even at cryogenic temperatures [10-21]. Prior research on the cryogenic deformation of austenitic steels has primarily involved static loading, with limited studies on dynamic loading, typically restricted to 77 K [11,12,19-24]. These studies have reported strain-induced martensitic transformation as the dominant deformation mechanism at cryogenic temperatures, forming ϵ and α ' martensite. However, a recent study by Xin et al. [16] did not observe strain-induced martensitic transformation during the ULT-fatigue testing of austenitic stainless steel at 4.2 K performed up to 30,000 cycles. Meanwhile, the tests did not provide information regarding the deformation mechanisms activated at higher strains or the

number of cycles to failure.

Therefore, a significant knowledge gap pertains to the response of these materials under dynamic loading at ULTs, which are crucial for applications such as liquid-hydrogen handling where the temperature can plummet to 20 K. Notably, despite over 80% of engineering failures being due to fatigue, data in this extreme regime remain scarce [25].

This study addresses a fundamental question: How do metals respond to fatigue loading under ultra-cryogenic conditions? Mechanical testing at such temperatures is vital for assessing material suitability in low-temperature applications. Unexpectedly, our investigation at 15 K revealed a remarkable paradox—a staggering 690% increase in the number of fatigue cycles to failure, even under approximately 86% higher loads compared to room temperature (RT) testing. We demonstrate that the exceptional properties observed in SS316L at ULT arise from the transition from singular (RT) to multiple deformation mechanisms (ULT), induced by the metastability of the γ -phase under low-temperature conditions. Our study not only advances the fundamental understanding of material behavior in extreme conditions, but it also carries practical cost-effective implications for emerging applications necessitating exceptional low-temperature performance.

E-mail address: sylee2012@cnu.ac.kr (S.Y. Lee).

^{*} Corresponding author.

2. Materials and methods

This study used industry-grade 316L austenitic stainless-steel plates, with the following chemical composition (wt. %): 17.58 Cr, 10.55 Ni, 1.99 Mo, 1.35 Mn, 0.24 Si, 0.09 Cu, 0.02 C, 0.05 N, < 0.001 S, < 0.001 P, and balance Fe. These plates were manufactured in accordance with American Society for Testing and Materials A240M/480M [26,27]. The rolled sheets were solution annealed at 1,050 °C and water quenched with final dimensions of 400 mm x 100 mm x 20 mm. The initial grain size was 46 \pm 15 μm . The dog bone-shaped cylindrical specimens for tensile and fatigue tests, with a gauge length of 12 mm and a gauge diameter of 6 mm, were machined, using a wire electrical discharge machine (EDM). Fractured samples were sectioned employing a wire EDM along the center for cross-sectional analysis.

2.1. Microstructure characterization

The specimens for microstructural characterization were prepared by metallographically polishing to a final surface finish of $0.05~\mu m$ using colloidal silica, followed by electrochemical polishing employing 35% (volume fraction) nital solution at RT. The fractography analysis was

performed on the fractured surface and cross-sectioned samples along the direction of crack propagation at multiple sites, as shown in Fig. 4 and Supplementary Figs. S(1 and 2). The selection of specimens tested at 1.3 times the yield strength for both RT and ULT for in-depth characterization was deliberate, as this condition resulted in an exceptional eight times higher fatigue life at ULT (nearly a 690% increase), even when subjected to an 86% higher maximum load, compared to RT-tested specimens (Fig. 1d). The microstructure characterization was performed using electron channeling contrast imaging (ECCI) and orientation mapping performed utilizing electron backscatter diffraction (EBSD). EBSD with a step size varying from 0.05 for fine scans to 0.5 for coarse scans was performed, employing a Carl Zeiss-Merlin Compact Scanning Electron Microscope equipped with Oxford-HKL NordlysNano at 20 kV. The orientation-mapping data was analyzed, using TSL-OIM Analysis v7 [28].

2.2. Mechanical characterization

Tensile testing at RT and ultra-low temperature, as well as fatigue testing at ultra-low temperature, were conducted, using a Servohydraulic Multipurpose Fatigue Testing Machine Walter Bai LVF-100-HH

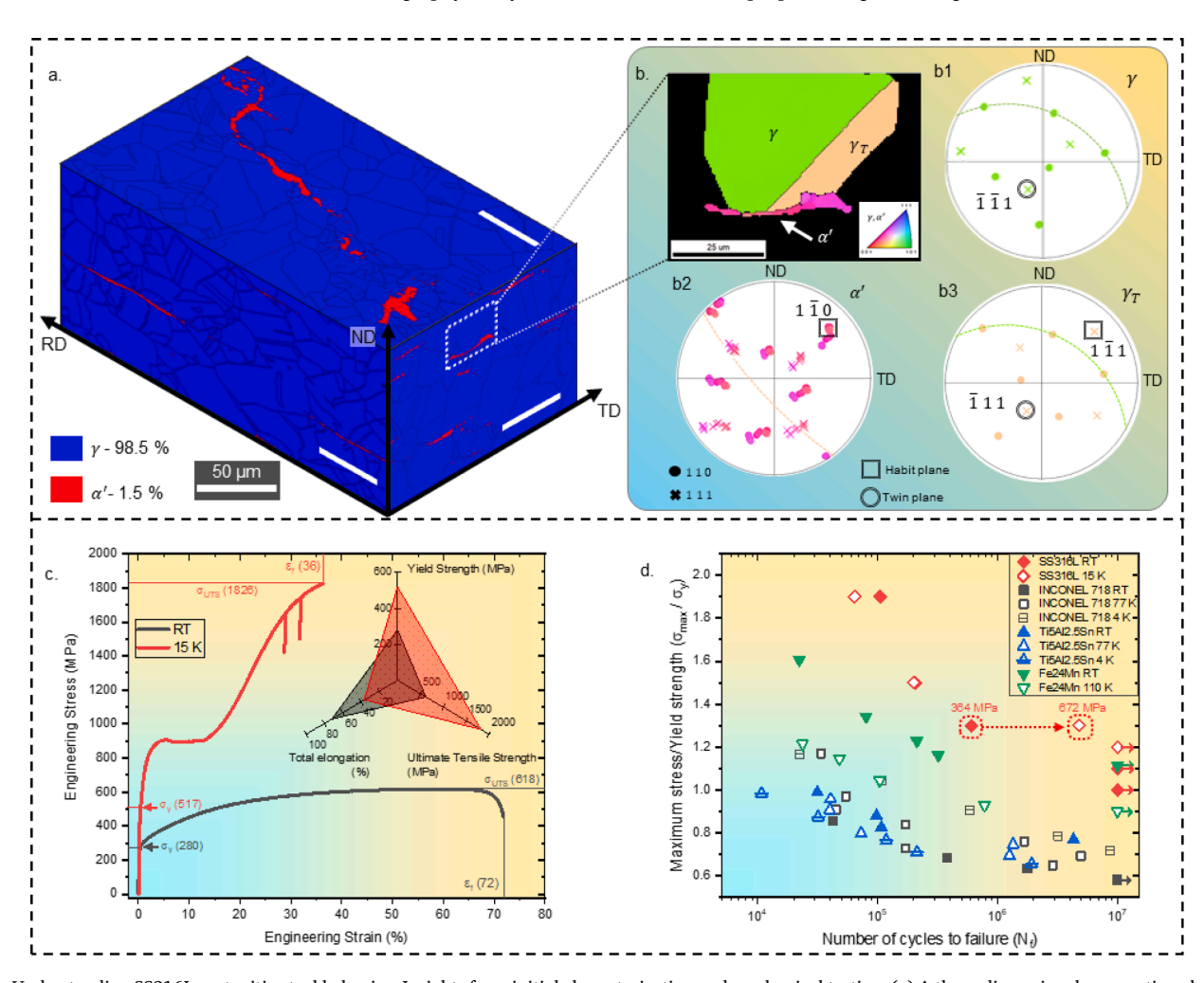


Fig. 1. Understanding SS316L austenitic-steel behavior: Insights from initial characterization and mechanical testing. (a) A three-dimensional perspective phase map representing the initial SS316L rolled sheets, providing insights into an α' -martensite morphology along the rolling direction (RD), transverse direction (TD), and normal direction (ND) planes. (b) Inverse Pole Figure (IPF) map of a grain highlighted within the white dashed box on the ND-TD plane in (a). Subsequent panels (b1-b3) present pole figures depicting the orientations of the γ parent, α' martensite, and γ_T -twinned grains within the highlighted region. (c) Tensile engineering stress-strain curves obtained from experiments conducted with the loading direction parallel to the RD, highlighting the material's response at both room temperature and ultra-low temperature (15 K), with the inset providing a comprehensive view of the mechanical properties. (d) Experimentally derived normalized maximum stress vs. the number of cycles to failure (S-N) curves, revealing fatigue life data obtained at room and cryogenic temperatures for SS316L (the present work), nickel-based superalloy (INCONEL 718) [31], alpha-titanium alloy (Ti5Al2.5Sn) [32], and high manganese steel (Fe24Mn) [19].

equipped with an Intelligent Service Group (ISG) cryogenic chamber cooled, using helium gas. RT-fatigue testing was carried out, using an Electroservo-Hydraulic MTS 810. The cryogenic chamber was vacuum sealed and flushed with He gas, a cycle repeated three times prior to cooling to avoid contamination in the chamber. Samples were cooled to 15 K over 10 hours, followed by 2 hours of homogenization. The specimens loaded in the fixture were maintained under a load-controlled mode to prevent the introduction of the external strain during cooling to ultra-low temperature. Throughout the testing, both sample and chamber temperatures were monitored. The same procedure, taking 12 hours, was employed for bringing the tested specimen back to RT. Tensile tests were performed at a constant initial strain rate of 5 x 10^{-5} $\rm s^{-1}$. The strain was calculated using a contact type clip-on extensometer with a strain limit of 50%, subsequent strain was obtained using the crosshead displacement. The yield strength was calculated using the 0.2% offset method. Load-controlled high-cycle fatigue testing with a sinusoidal waveform was conducted with a minimum to maximum stress ratio, R of 0.1, and a frequency of 10 Hz at a maximum load ranging from 1.0 to 1.9 times yield strength at respective temperatures. Highcycle fatigue tests were stopped after 10⁷ cycles, and the surviving samples were labeled run-outs.

3. Results

3.1. Initial microstructural analysis and mechanical properties

The electron backscatter diffraction (EBSD) phase maps along the rolling direction (RD), transverse direction (TD), and normal direction (ND) revealed that the initial material contains about 1.5% of residual α martensites elongated along the RD and flattened along the TD due to the strain induced during rolling (Fig. 1a). The inverse pole figure map on the ND-TD plane shows the α' flattened along TD (Fig. 1b). We employed pole figures to identify the crystallographic characteristics of the parent grain, γ , twinned grain, γ_T and α' phases [29]. These figures, in Figs. 1b(1-3), highlight the close-packed planes and directions with their respective symbols. A comparison of Figs. 1b(1-3) reveals a $\sum 3$ twin relationship between γ and γ_T achieved through a 60° rotation along the $[\overline{1} \ \overline{1} \ 1]_{\nu}$ axis. These annealing twins result from the thermomechanical-processing history of the initial material [30]. Importantly, γ exhibits no orientation relationship with α' , whereas $(1\overline{1}1)_{\gamma_{\tau}}//(1\overline{1}0)_{\alpha}$ serves as the habit plane for transformation with no parallel close-packed direction.

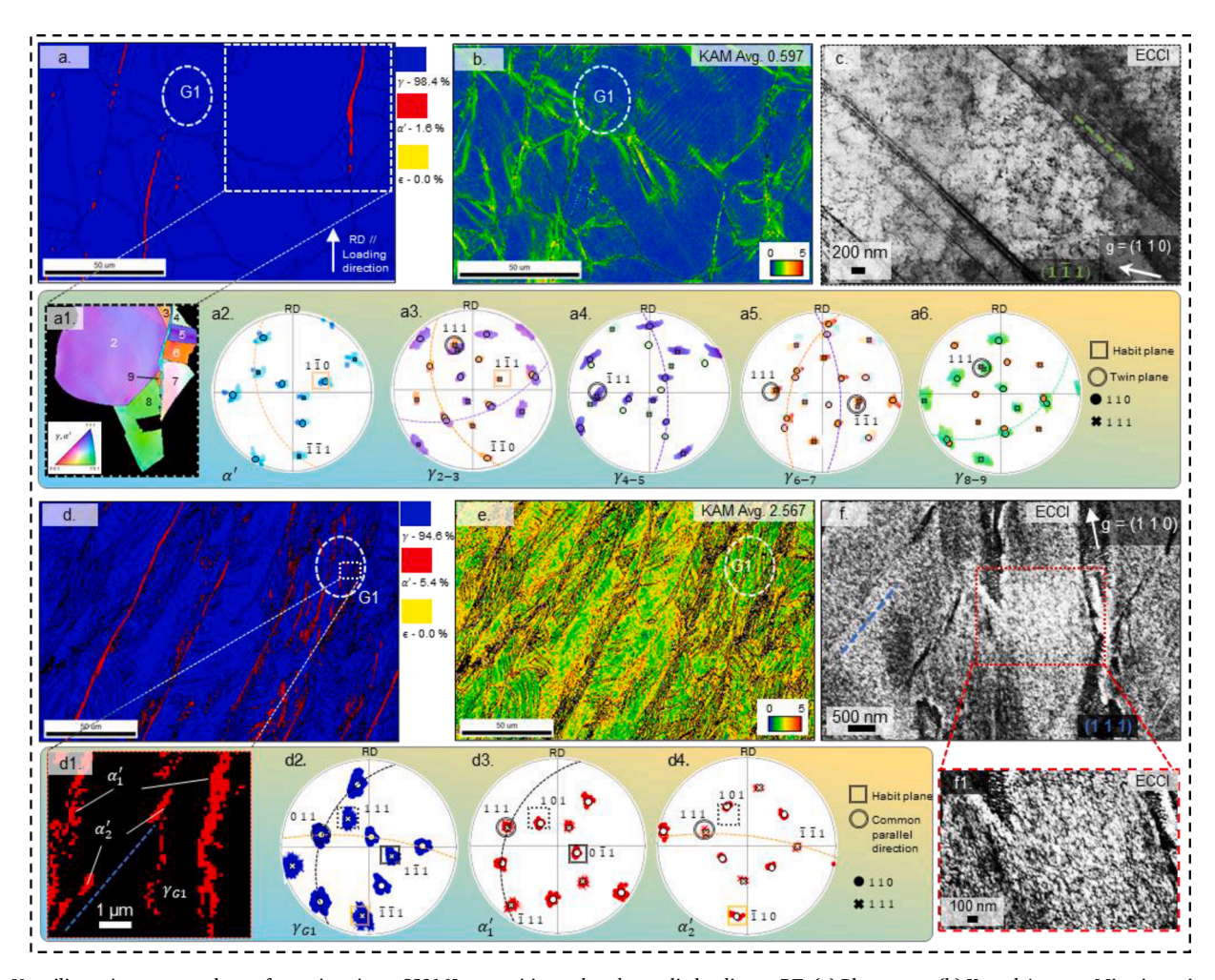


Fig. 2. Unveiling microstructural transformations in an SS316L austenitic steel under cyclic loading at RT. (a) Phase map. (b) Kernel Average Misorientation (KAM) of the cross-section of a crack-propagation-rupture interface, highlighted in Fig. S1b. (c) Inverted ECCI image of the grain, G1, as highlighted in (a, b), showing a trace of the highest Schmid factor slip system. Depicted in (a1) is an IPF map of the grains G(2-9) surrounding the α' martensite, as highlighted in (a). [a(2-6)] pole figure showcasing the crystal orientation with the corresponding IPF color of (a2) α' martensite and [a(3-6)] γ-matrix grains, underlining the Kurdjumov-Sachs relationship satisfied by the α' martensite and γ_3 grain in addition to the strained twin relationship among the γ_{2-3} , γ_{5-6} , γ_{6-7} , and γ_{8-9} . (d) Phase map. (e) KAM of the cross-section of the rupture region, highlighted in Fig. S1c. (f) Inverted ECCI image of the grain, G1, as highlighted in (d, e), showing a trace of the highest Schmid factor slip system. Depicted in (d1) is a phase map of the grain G1, highlighted in (d). [d(2-4)] pole figure displaying the crystal orientation of γ_{G1} , α_1 , and α_2 , underlining the Kurdjumov-Sachs relationship on two {1 1 1} $_{\gamma_{G1}}$ planes. (f1) Inverted ECCI images presenting the dense dislocation-cell formation.

At ULT, the material displayed an 86% increase in yield strength and a substantial 195% increase in ultimate tensile strength, albeit with a 49% reduction in ductility, as compared to RT (Fig. 1c). This trend led to an overall 11% improvement in tensile toughness, compared to RT. The maximum stress normalized by yield strength vs. number of cycles to failure plot demonstrates a significantly higher normalized stress for a given number of cycles to failure for SS316L, as compared to a nickelbased superalloy [31], an alpha-titanium alloy [32], and high-manganese steel [19] (Fig. 1d). Furthermore, at ULT, there is a notable increase in the number of cycles to failure at a normalized stress ratio of 1.3, compared to RT for SS316L (Fig. 1d).

3.2. Room-Temperature Fatigue Mechanisms

At the crack-propagation-rupture interface (highlighted in Fig. S1b), the cross-sectional EBSD-phase map (Fig. 2a) reveals α' elongated along the RD, with a phase fraction similar to the initial material, suggesting that the observed α' originates from the initial material. Examining the highlighted region (Fig. 2a1), we explored the crystallographic characteristics of the α' martensite and neighboring γ grains [Figs. 2a(2-6)]. There is no orientation relationship between α' and γ grains, except for

 γ_3 , which tends to satisfy a strained Kurdjumov-Sachs (K-S) [33] relationship [(1 $\overline{1}$ 1) $_{\gamma_3}$ // (1 $\overline{1}$ 0) $_{\alpha}$, [$\overline{1}$ $\overline{1}$ 0] $_{\gamma_3}$ // [$\overline{1}$ $\overline{1}$ 1] $_{\alpha}$] [Figs. 2a(2,3)]. Furthermore, a \sum 3 twin relationship is observed among the γ grains, specifically, γ_{2-3} , γ_{5-6} , γ_{6-7} , and γ_{8-9} . The Kernel Average Misorientation (KAM) map (Fig. 2b) reveals strain localization along a preferred orientation inside grains. A high-magnification inverted electron channeling contrast image (ECCI) of the grain, G1 (Fig. 2c), demonstrates strain localization on the slip system, which has the highest Schmid factor, specifically (1 $\overline{1}$ 1)[1 0 $\overline{1}$]. This area also displays nascent dislocation-cell formation, with a cell size of approximately 500 nm (Fig. 2c). The spread in orientations visible in the pole figures [Figs. 2a (2-6)] for γ and α' grains indicate crystal rotation due to plastic deformation [29]. The spread in the orientation is not uniform, and is due to one dominant slip system (Fig. 2c), resulting in strain localization (Fig. 2b).

In the rupture region cross-section (highlighted in Fig. S1c), the α -phase fraction increased to around 5.4% (Fig. 2d), indicating that even at RT, the $\gamma \rightarrow \alpha'$ phase transformation occurs at higher strain levels. The KAM map shows increased residual strains due to higher deformation in this region (Fig. 2e). A more detailed phase map of the highlighted region (Fig. 2d1) reveals two variants of α' : coarser α'_1 satisfying a

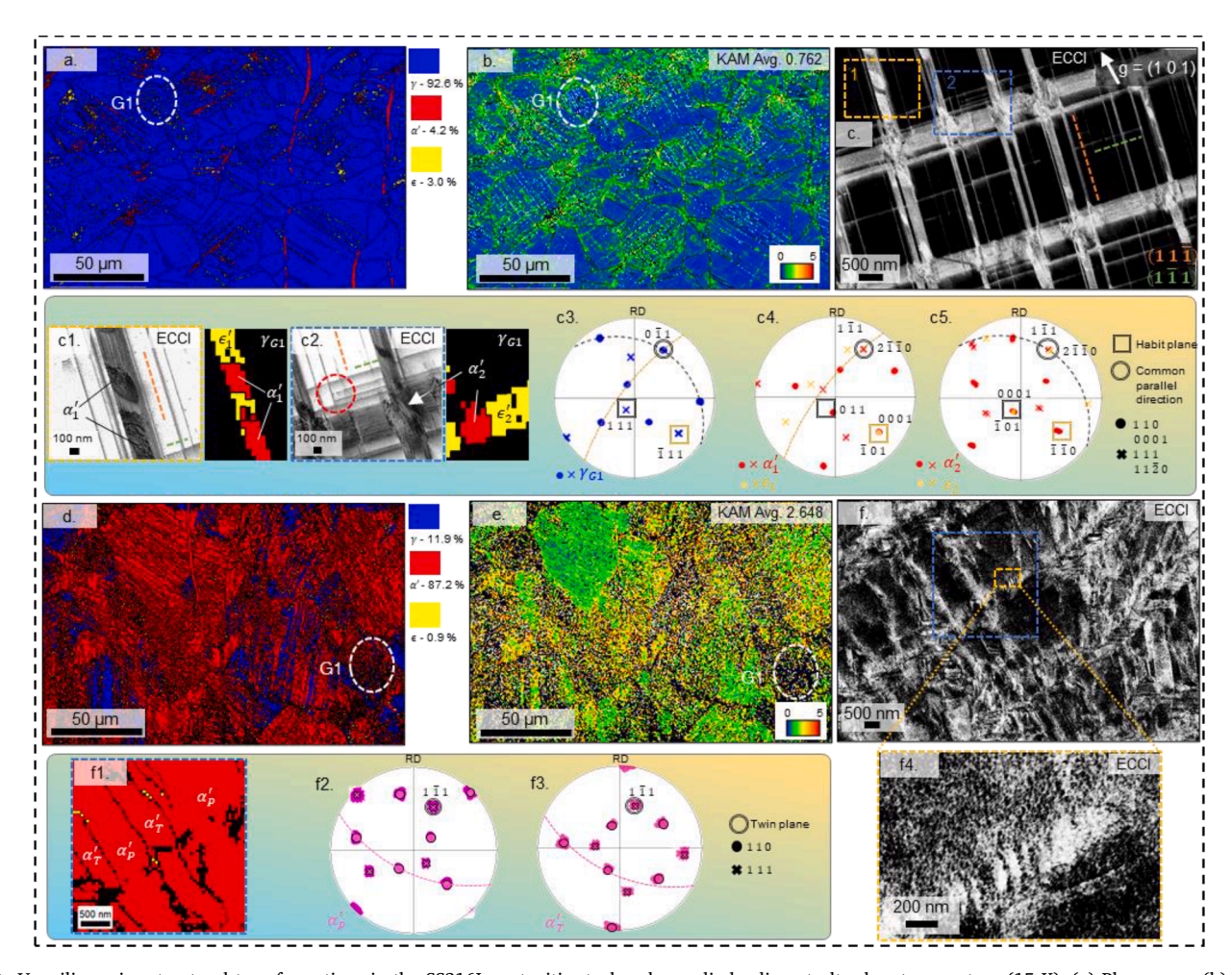


Fig. 3. Unveiling microstructural transformations in the SS316L austenitic steel under cyclic loading at ultra-low temperature (15 K). (a) Phase map. (b) Kernel Average Misorientation (KAM) map of the cross-section of crack-propagation-regions interface highlighted in Fig. S2b. (c) ECCI image of the grain, G1, as highlighted in (a, b). Depicted in (c1), an inverted ECCI image and a phase map of the region enclosed by the yellow box in (c) revealing the α'_1 martensite formed on a single ϵ_1 martensite. (c2), An inverted ECCI image and phase map of the region within the blue box in (c) shows the α'_2 martensite formed at the intersection of ϵ_1 and ϵ_2 martensites. [c(3-5)] Pole figures displaying the crystal orientation of the (c3) γ matrix, (c4) α'_1 and ϵ_1 ,(c5) α'_2 and ϵ_2 , underlining orientation relationships. (d) Phase map. (e) KAM of the cross-section of the rupture region, highlighted in Fig. S2d. (f) ECCI image of grain, G1, as highlighted in (d, e). Depicted in (f1) is the phase map of the area highlighted by a blue box in (f). [f(2-3)] Pole figure displaying the crystal orientation of the α' parent and twinned region. (f4) ECCI image of the region highlighted in (f).

K-S [33] relationship [(1 $\overline{1}$ 1) $_{\gamma_1}$ // (0 $\overline{1}$ 1) $_{a_1'}$, [0 1 1] $_{\gamma_1}$ // [1 1 1] $_{a_1'}$] with the matrix and finer a_2' martensite maintaining a different K-S [33] relationship [($\overline{1}$ $\overline{1}$ 1) $_{\gamma_1}$ // ($\overline{1}$ 1 0) $_{a_2'}$, [0 1 1] $_{\gamma_1}$ // [1 1 1] $_{a_2'}$]. In addition, the martensite variants exhibit planes of (1 0 1) $_{a_1'}$ and (1 0 1) $_{a_2'}$ almost parallel to the (1 1 1) $_{\gamma_1}$ plane with the highest Schmid factor, revealing that $a_{1/2}'$ maintains a K-S relationship with two {1 1 1} $_{\gamma_1}$ planes as habit planes. This orientation relationship aligns with findings in the literature, where one of the {1 1 1} $_{\gamma}$ planes is the primary slip plane, and the other is a conjugate or cross-slip plane [34,35], and a' forms at the intersection of dislocation walls formed on {1 1 1} $_{\gamma}$ planes [36]. Dense dislocation-wall formation is evident in the inverted ECCI image in Fig. 2f1.

3.3. Ultra-low Temperature Fatigue Mechanisms

At the interface in the crack-propagation regions (highlighted in Fig. S2b), the EBSD phase map (Fig. 3a) reveals increased ϵ and α' phase fractions, approximately 3.0% and 4.2%, respectively. In addition to the elongated morphology, nanometer-sized fine α' grains are also observed [Fig. 3(a, c)]. The KAM map (Fig. 3b) indicates strain localization along preferred planes within each grain. The ECCI image of the grain, G1 (Fig. 3c), clarifies that the strain localization in the KAM map aligns with bands formed parallel to the traces of $\{1\ 1\ 1\}_{\gamma_{G1}}$ planes, specifically the $(1\ 1\ \bar{1})$ and $(1\ \bar{1}\ 1)$ planes, showing the highest and second highest Schmid factor.

The high-magnification inverted ECCI images and EBSD-phase maps in Figs. 3c1 andc2 of regions 1 and 2 in Fig. 3c, respectively, reveal that these bands consist of deformation-induced ϵ martensite. The $\gamma \rightarrow \epsilon$ transformation occurs through the gliding of Shockley partial dislocations on every second $\{1\ 1\ 1\}_{\gamma}$ plane [37]. Stacking faults resulting from partial dislocations along high Schmid factor slip planes are also visible in Figs. 3c(1 and 2). Dislocation junctions, which appear to be Lomer-Cottrell locks, are highlighted in red in Fig. 3c2. Nano-sized α' grains appear on the ϵ bands, indicating $\gamma \rightarrow \epsilon \rightarrow \alpha'$ phase transformation [18,29,38-40]. The α'_1 martensite forms in a single ϵ_1 band (Fig. 3c1), while the α'_2 martensite forms at the intersection of ϵ_1 and ϵ_2 bands (Fig. 3c2).

Comparing the pole figures between the parent, γ_{G1} (Fig. 3c3), and ϵ_1 , α_1' phases (Fig. 3c4) reveal a Shoji-Nishiyama[41] (S-N) relationship [($\overline{1}$ 1 $1)_{\gamma_{G1}}//(0$ 0 0 1) $_{\epsilon_1}$, [0 $\overline{1}$ 1] $_{\gamma_{G1}}//[2$ $\overline{1}$ $\overline{1}$ 0] $_{\epsilon_1}$] between $\gamma_{G1} - \epsilon_1$, K-S [33] relationship [($\overline{1}$ 1 1) $_{\gamma_{G1}}//(\overline{1}$ 0 1) $_{\alpha_1'}$, [0 $\overline{1}$ 1] $_{\gamma_{G1}}//(\overline{1}$ $\overline{1}$ 1] $_{\alpha_1'}$] between $\gamma_{G1} - \alpha_1'$, and Burgers [42] relationship [(0 0 0 1) $_{\epsilon_1}//(\overline{1}$ 0 1) $_{\alpha_1'}$, [2 $\overline{1}$ $\overline{1}$ 0] $_{\epsilon_1}//[1$ $\overline{1}$ 1] $_{\alpha_1'}$] between $\epsilon_1 - \alpha_1'$. Similar orientation relationships [S-N [41], K-S [33], and Burgers [42]] exist among γ_{G1} , ϵ_2 , and α_2' [Figs. 3c(3,5)] [(1 1 1) $_{\gamma_{G1}}//(0$ 0 0 1) $_{\epsilon_2}//(\overline{1}$ 0 1) $_{\alpha_2'}$, [0 $\overline{1}$ 1] $_{\gamma_{G1}}//(2$ $\overline{1}$ $\overline{1}$ 0] $_{\epsilon_2}//[1$ $\overline{1}$ 1] $_{\alpha_2'}$] . Notably, all these phase transformations ($\gamma_{G1} \rightarrow \epsilon_{1/2} \rightarrow \alpha_{1/2}'$) share the same close-packed direction [0 $\overline{1}$ 1] $_{\gamma_{G1}}$, exhibiting the smallest Schmid factor with (1 1 1) $_{\gamma_{G1}}$ and ($\overline{1}$ 1 1) $_{\gamma_{G1}}$ planes. It is also notable that both α_1' and α_2' tend to satisfy a K-S [33] relationship with two {1 1 1} $_{\gamma_{G1}}$ planes.

In the rupture region (highlighted in Fig. S2d), the cross-sectional EBSD-phase map (Fig. 3d) reveals that the majority of the initial γ phase has transformed into α' (\sim 87%), with a reduced ϵ phase fraction, compared to the crack-propagation-regions interface. This reduction indicates that ϵ is an intermediate phase that transforms to α' under higher strains [29,35,38,43]. The KAM map shows the increased residual strain due to higher plastic deformation in this region (Fig. 3e). The high-magnification ECCI image (Fig. 3f) and phase map (Fig. 3f1) of the grain, G1, indicate deformation products formed within the α' grains.

The crystallographic-orientation information, presented as pole figures of the parent grain (α_P' , Fig. 3f2), and the transformed area (α_T' , Fig. 3f3) demonstrates a $\sum 3$ twin relationship between the two via a 60° rotation along the $[1\ \overline{1}\ 1]_{\alpha'}$ axis, signifying that the α' formed further deforms via twinning. Additionally, the high-magnification ECCI image (Fig. 3f1) reveals dense dislocation-cell formation.

3.4. Fractography of RT and ULT Fatigue-Fractured Specimens

The SEM images of the fatigue-fractured surfaces at RT and ULT are presented in Fig. 4. Both the RT and ULT specimens exhibited three distinct zones on the fracture surface: (1) the crack-initiation site, (2) the crack-propagation zone, and (3) the rupture zone.

Comparative analysis of the RT- and ULT-fractured specimens revealed three key differences: (1) In RT specimens, microcracks were oriented perpendicular to the crack-propagation direction, while in ULT specimens, microcracks consistently aligned along the TD (Fig. S2a1), irrespective of the crack-propagation direction. (2) The crack-propagation region in the ULT specimens exhibited two sub-regions based on surface topography, with varying void frequencies and surface-slope steepness (Fig. S2). In both regions, micro-cracks and voids elongated along the TD. (3) Striations were observed in RT-fractured specimens but not in ULT specimens.

High-magnification SEM images of selected regions along the crackpropagation direction are shown in Figs. 4a(1-6) for RT and Figs. 4b(1-6) for ULT specimens. In the RT-fractured specimen, striations became visible after approximately 1 mm from the crack-initiation site [Fig. 4 (a1,2)], with a spacing of around 100 nm. Further along the crack propagation, similar striation cracks emerged along with microvoids (Fig. 4a), presenting an increased striation spacing of around 270 nm (Fig. 4a3). On the crack-propagation side of the interface [Fig. 4(a,a4)], more frequent voids were visible, along with increased striation spacing, approximately 950 nm. The inset of Fig. 4a4 illustrates the mechanism of striation-crack formation; nucleation of nanovoids along striations. followed by void coalescence, leading to striation cracks nucleation and propagation. In the rupture side of the crack-propagation-rupture interface, voids/poorly formed dimples with blunt edges ranging from a few hundred nanometers to a few hundred micrometers in size were elongated perpendicular to the crack-propagation direction (Fig. 4a5). Finally, in the rupture zone, there were large shear dimples surrounded by finer shear dimples with sharp edges oriented along the direction of crack propagation (Fig. 4a6).

For the ULT-fractured specimens, microcracks initially sized around $1 \sim 10 \, \mu m$ and aligned parallel to the TD were visible at an approximate distance of 500 µm from the crack-initiation site (Fig. 4b1). These microcracks grew larger as the crack propagated. On one side of the crackpropagation sub-zones interface, the larger cracks reached a size of a few hundred micrometers (Fig. 4b). Importantly, the direction of these microcracks remained constantly parallel to the TD, independent of the crack-propagation direction (Fig. 4b2). Higher-magnification images of the region around these microcracks (Fig. 4b3) revealed the presence of nano-sized voids/blunt dimples. On the opposite side of the crackpropagation sub-zones interface, larger voids/blunt dimples were elongated along the TD direction (Fig. 4b), with the surrounding area featuring finer micron-sized shear dimples elongated along the direction of crack propagation (Fig. 4b4). Further along the crack propagation, the size of similar micron-sized shear dimples increased (Fig. 4b5). In the rupture zone, fine equiaxed micron-sized dimples with sharp edges, akin to the tensile fracture, were visible (Fig. 4b6).

4. Discussion

This discussion elucidates the reasons for the remarkable increase in fatigue life at ULT, compared to RT, despite higher applied loads at ULT. The higher yield strength at ULT is primarily due to increased thermal-

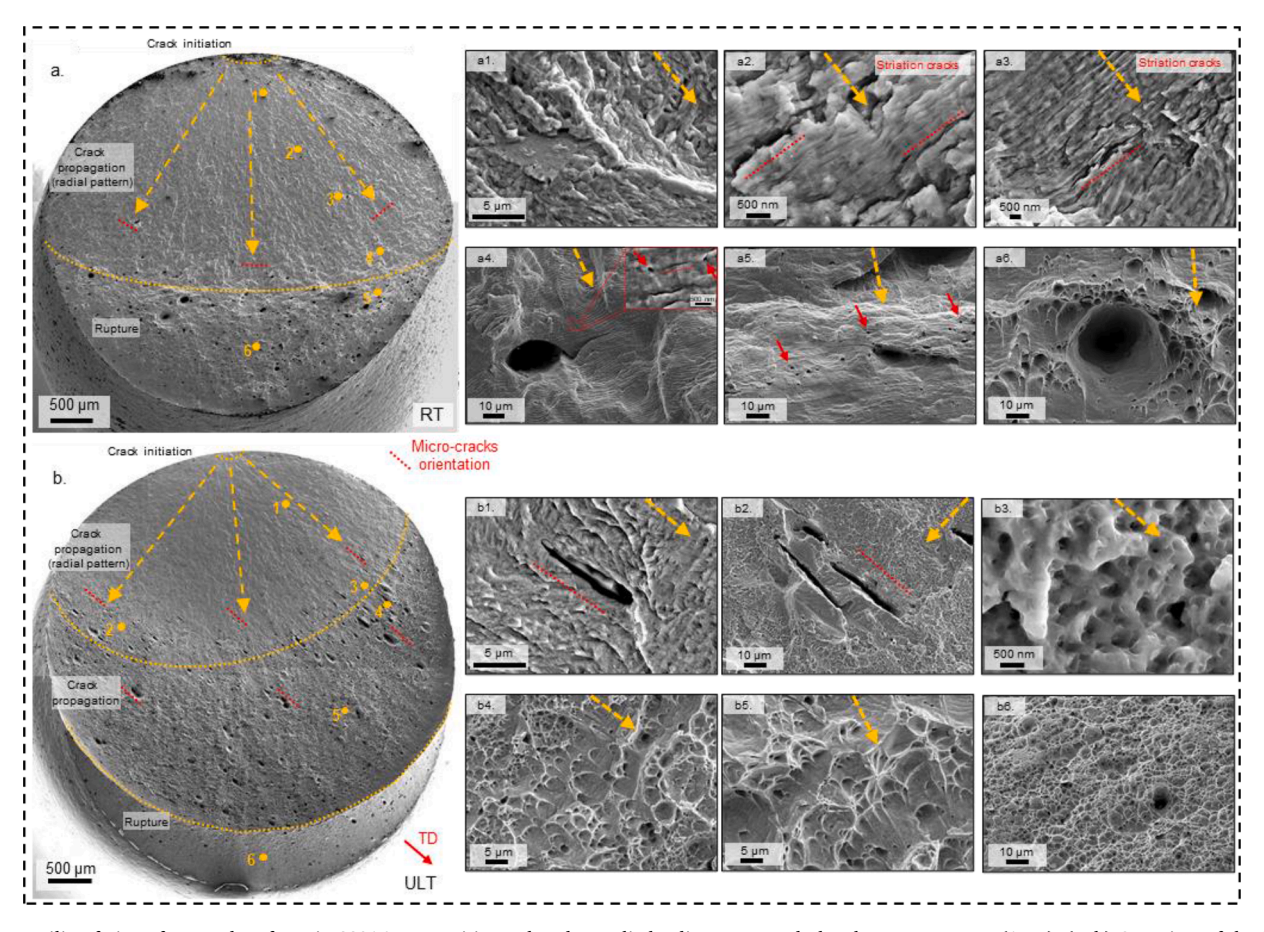


Fig. 4. Unveiling fatigue-fractured surfaces in SS316L austenitic steel under cyclic loading at RT and ultra-low temperature (15 K). (a, b) Overview of the fatigue-fractured surface at RT and 15 K, respectively, highlighting the exhibited three distinct zones: the crack-initiation site, crack-propagation zone, and rupture zone. High-magnification SEM images of the sites in the [a(1-4)] crack-propagation zone, [a(5, 6)] rupture zone at RT showing serration cracks perpendicular to the direction of crack propagation, void and dimple formation, respectively. High-magnification SEM images of the sites in the [b(1-3)] region, one of the crack-propagation zones, [b(4, 5)] region two of the crack-propagation zone, and (b6) the rupture zone at ULT showing microcracks parallel to the transverse direction, void formation, and shear-dimple formation, respectively.

strengthening effects like the increased Peierls stress, dependent on short-range core interaction [44,45]. At cryogenic temperatures (15K), deformation-induced martensitic transformation occurs in austenitic stainless steels during monotonic tension due to a decrease in the stacking fault energy (SFE). The reduced barrier of stacking faults enables various deformation mechanisms, leading to the improved tension behavior [20]. Specifically, Niessen et al.'s [46] ab initio study quantifies the intrinsic stacking fault energy of paramagnetic γ -Fe and austenitic stainless steels based on magnetic properties. However, unlike monotonic tension, internal friction during cyclic loading can dissipate energy from heating the sample, influencing magnetic properties. Thus, investigating the underlying mechanisms of fatigue at 15 K becomes crucial for advancement in ULT magnetic applications.

The impressive increase in fatigue life at ULT, as compared to RT (Fig. 1d), aligns qualitatively with the observed enhancement in tensile toughness (Fig. 1c). These findings can be attributed to the variation in the deformation mechanisms activated at ULT, as revealed by the cross-sectional microstructural analysis.

A crucial contributing factor to this behavior is the substantially higher ultimate tensile strength at ULT, almost 195% greater than at RT (Fig. 1c). Consequently, the reduced probability of stress reaching the threshold required for crack nucleation contributed to the increased fatigue life. In the crack-propagation zone at RT, planar slip led to strain localization along the $\{1\ 1\ 1\}_{\gamma}$ planes [Figs. 2(b, c)], resulting in striation cracking perpendicular to the crack-propagation direction [47]. Contrastingly, at ULT, microcracks were initiated at the initial $\alpha^{'}$ – γ

interfaces, aligning parallel to the TD (Fig. S2a1). This trend suggests that the initial $\alpha' - \gamma$ interface, which does not follow any orientation relation, is incoherent and weaker at ULT. Plastic deformation at ULT is accommodated through the formation of stacking-fault bundles parallel to the $\{1\ 1\ 1\}_{r}$ planes [20], embedded among the ϵ , also parallel to the $\{1\ 1\ 1\}_{\nu}$ planes (Fig. 3c). The ϵ martensite further transforms into α' variants via single and double shear mechanisms [18,22,29,35,37-40, 43], while maintaining a semi-coherent interface (Fig. 3c). The two-step phase-transformation mechanism $(\gamma \rightarrow \epsilon \rightarrow \alpha')$ at ULT enhances the utilization of the applied plastic strain during fatigue cycles, subsequently reducing the crack-propagation rate, compared to RT. Additionally, the $\gamma \rightarrow \alpha'$ phase transformation introduces compressive stresses, resulting in the crack-closure phenomenon [21,48], and the transformation from the softer γ to harder α' provides hardening [21]. This hardening behavior delays strain localization and necessitates higher stresses for crack propagation, further decreasing the crack-propagation rate.

At the rupture site, a minor $\gamma \rightarrow \alpha'$ phase transformation occurs at RT (Fig. 2d). However, this feature is quantitatively less significant than the transformation observed at ULT ($\gamma \rightarrow \epsilon \rightarrow \alpha'$). At ULT, the transformed α' phase also undergoes $\sum 3$ twinning [Figs. 3f(1-3)], further accommodating the applied strain during fatigue cycles. However, the major factor contributing to the enhanced fatigue life at ULT is transformation-induced plasticity, as the enhancement was relatively less during fatigue tests conducted at higher stresses (1.5 and 1.9 times σ_{ys}), likely due to the phase transformation occurring during initial loading, even before

the onset of fatigue.

5. Conclusions

In summary, the increased fatigue life at ULT is due to the effective fatigue strain utilization retarding crack propagation through multiple deformation mechanisms, specifically stacking faults, two-step martensitic phase transformation $(\gamma \rightarrow \epsilon \rightarrow \alpha')$, and α' twinning. The reduced crack-propagation rates, the compressive effect of phase transformation, and the intrinsic material properties at ULT present exciting possibilities for sustainable high-performance materials in ultra-cryogenic applications.

Funding

National Research Foundation (NRF) grant funded by the Korean government (2021R1A4A1031494, 2023R1A2C2007190), National Science and Technology Council (NSTC) Grants NSTC 112-2221-E-A49-027 and 112-2811-E-A49-521, National Science Foundation (DMR –1611180, 1809640, and 2226508), Army Research Office (W911NF-13–1-0438 and W911NF-19–2-0049).

CRediT authorship contribution statement

Chetan Singh: Writing – original draft, Visualization, Software, Methodology, Investigation, Formal analysis, Data curation. Taeho Lee: Resources, Methodology. Keun Hyung Lee: Resources, Methodology. You Sub Kim: Resources, Methodology. E-Wen Huang: Writing – review & editing, Validation. Jayant Jain: Writing – review & editing, Validation. Soo Yeol Lee: Writing – review & editing, Supervision, Resources, Project administration, Funding acquisition, Conceptualization.

Declaration of competing interest

We (Dr. Chetan Singh, Mr. Taeho Lee, Mr. Keun Hyung Lee, Mr. You Sub Kim, Prof. E-Wen Huang, Prof. Jayant Jain, Prof. Peter K. Liaw, and Prof. Soo Yeol Lee) confirm that there are no conflicts of interest to declare. No similar work has been published or is under consideration elsewhere.

Data availability

Data will be made available on request.

Acknowledgments

The authors thank the Chungnam National University for providing the infrastructural support and a scanning electron microscope equipped with a backscattered electron detector for electron channeling contrast imaging and electron backscattered diffraction detector.

Supplementary materials

Supplementary material associated with this article can be found, in the online version, at doi:10.1016/j.apmt.2024.102195.

References

- [1] J. Rackwitz, Q. Yu, Y. Yang, G. Laplanche, E.P. George, A.M. Minor, R.O. Ritchie, Acta Mater. 200 (2020) 351–365.
- [2] P. Kumar, M. Michalek, D.H. Cook, H. Sheng, K.B. Lau, P. Wang, M. Zhang, A. M. Minor, U. Ramamurty, R.O. Ritchie, Acta Mater. 258 (2023) 119249.
- [3] D. Liu, Q. Yu, S. Kabra, M. Jiang, P. Forna-Kreutzer, R. Zhang, M. Payne, F. Walsh, B. Gludovatz, M. Asta, A.M. Minor, E.P. George, R.O. Ritchie, Science 378 (2022) 978–983.
- [4] Y.H. Jo, S. Jung, W.M. Choi, S.S. Sohn, H.S. Kim, B.J. Lee, N.J. Kim, S. Lee, Nat. Commun. 1 (8) (2017) 1–8, 2017 8:.
- [5] B. Gludovatz, A. Hohenwarter, K.V.S. Thurston, H. Bei, Z. Wu, E.P. George, R. O. Ritchie, Nat. Commun. 7 (1) (2016) 1–8, 20167.
- [6] Z. Li, K.G. Pradeep, Y. Deng, D. Raabe, C.C. Tasan, Nature 534 (2016) 227–230.
- [7] M. Naeem, H. He, S. Harjo, T. Kawasaki, F. Zhang, B. Wang, S. Lan, Z. Wu, Y. Wu, Z. Lu, C.T. Liu, X.L. Wang, Scr. Mater. 188 (2020) 21–25.
- [8] X. Wen, L. Zhu, M. Naeem, H. Huang, S. Jiang, H. Wang, X. Liu, X. Zhang, X. L. Wang, Y. Wu, Z. Lu, Scr. Mater. 231 (2023) 115434.
- [9] K. Cui, P.K. Liaw, Y. Zhang, Metals 12 (2022) 2075.
- [10] J.G. Weisend, V. Flynn, E. Thompson, A Reference Guide for Cryogenic Properties of Materials [No. SLAC-TN-03-023], CA, United States, 2003.
- [11] W. Han, Y. Liu, F. Wan, P. Liu, X. Yi, Q. Zhan, D. Morrall, S. Ohnuki, J. Nucl. Mater. 504 (2018) 29–32.
- [12] O. Umezawa, T. Ogata, T. Yuri, K. Nagai, K. Ishikawa, R.P. Reed, F.R. Fickett, L. T. Summers, M. Stieg, Advances in Cryogenic Engineering Materials, 40, Springer US, Boston, MA, 1994, pp. 1231–1238. Part A.
- [13] P. Kumar, R. Jayaraj, J. Suryawanshi, U.R. Satwik, J. McKinnell, U. Ramamurty, Acta Mater. 199 (2020) 225–239.
- [14] T.S. Byun, N. Hashimoto, K. Farrell, Acta Mater. 52 (2004) 3889-3899.
- [15] F. De Backer, V. Schoss, G. Maussner, Nucl. Eng. Design 206 (2001) 201-219.
- [16] J. Xin, H. Zhang, W. Sun, W. Wang, D. Wu, B. Lyu, F. Shen, Z. Fang, C. Huang, L. Li, Scr. Mater. 226 (2023).
- [17] X. Xie, D. Ning, J. Sun, Mater. Charact. 120 (2016) 195-202.
- [18] C. Luo, H. Yuan, Acta Mater. 238 (2022).
- [19] D.H. Jeong, S.G. Lee, W.K. Jang, J.K. Choi, Y.J. Kim, S. Kim, Metall. Mater. Trans. A Phys. Metall. Mater. Sci. 44 (2013) 4601–4612.
- [20] S. Li, P.J. Withers, S. Kabra, K. Yan, Mater. Sci. Eng. A 880 (2023) 145279.
- [21] H. Maharaja, B. Das, A. Singh, S. Mishra, Int. J. Fatigue 166 (2023).
- [22] C. Garion, B. Skoczeń, S. Sgobba, Int J Plast 22 (2006) 1234-1264.
- [23] Y. Wang, Y. Zhang, A. Godfrey, J. Kang, Y. Peng, T. Wang, N. Hansen, X. Huang, Commun. Mater. 2 (1) (2021) 1–10, 2 (2021).
- [24] K. Nalepka, B. Skoczeń, M. Ciepielowska, R. Schmidt, J. Tabin, E. Schmidt, W. Zwolińska-Faryj, R. Chulist, Materials 14 (2020) (2021) 127. Page 127 14.
- [25] S. Suresh, Fatigue of Materials, Cambridge University Press, 1998.
- [26] Standard Specification for Chromium and Chromium-Nickel Stainless Steel Plate, Sheet, and Strip for Pressure Vessels and for General Applications, 2023.
- [27] Standard Specification for General Requirements for Flat-Rolled Stainless and Heat-Resisting Steel Plate, Sheet, and Strip, 2022.
- [28] Gatan, 2023.
- [29] N. Nakada, H. Ito, Y. Matsuoka, T. Tsuchiyama, S. Takaki, Acta Mater. 58 (2010) 895–903.
- [30] R.A. Varin, J. Kruszynska, Acta Metall. 35 (1987) 1767–1774.
- [31] Y. Ono, T. Yuri, H. Sumiyoshi, E. Takeuchi, S. Matsuoka, T. Ogata, Mater. Trans. 45 (2004) 342–345.
- [32] Y. Ono, T. Yuri, H. Sumiyoshi, S. Matsuoka, T. Ogata, Cryogenics (Guildf) 43 (2003) 483–489.
- [33] G. Kurdjumow, G. Sachs, Zeitschrift Für Physik 64 (1930) 325–343.
- [34] Y. Matsuoka, T. Iwasaki, N. Nakada, T. Tsuchiyama, S. Takaki, ISIJ International 53 (2013) 1224–1230.
- [35] Y. He, J. Gao, Y. He, K. Shin, J. Mater. Sci. 57 (2022) 5230-5240.
- [36] G. Miyamoto, N. Iwata, N. Takayama, T. Furuhara, Acta Mater. 60 (2012) 1139–1148.
- [37] G.B. Olson, M. Cohen, J. Less Common. Metals 28 (1972) 107-118.
- [38] J.L. Wang, M.H. Huang, X.H. Xi, C.C. Wang, W. Xu, Mater. Charact. 163 (2020).
- [39] X.S. Yang, S. Sun, X.L. Wu, E. Ma, T.Y. Zhang, Sci Rep 4 (2014).
- [40] T.H. Lee, H.Y. Ha, J.Y. Kang, J. Moon, C.H. Lee, S.J. Park, Acta Mater. 61 (2013) 7399–7410.
- [41] Zenji Nishiyama, Martensitic Transformation, Elsevier, 2012.
- [42] W.G. Burgers, Physica 1 (1934) 561–586.
- [43] Y. Tian, A. Borgenstam, P. Hedström, J. Alloys Compd. 766 (2018) 131–139.
- [44] I.C. Jung, B.C. De Cooman, Acta Mater. 61 (2013) 6724–6735.
- [45] R.P. Reed, N.J. Simon, Adv. Cryog. Eng. (1984) 127-136.
- [46] F. Niessen, W. Li, K.V. Werner, S. Lu, L. Vitos, M. Villa, M.A.J. Somers, Acta Mater. 253 (2023).
- [47] K. Tanaka, T. Mura, Acta Metall. 32 (1984) 1731–1740.
- [48] J.M. Alves, A. dos Santos Paula, L.P. Brandao, Mater. Research 24 (2021) e20210156.